Vibrational properties of hexagonal $Ge_2Sb_2Te_5$ from first principles

2009 J. Phys.: Condens. Matter 21 245401

(http://iopscience.iop.org/0953-8984/21/24/245401)

J. Phys.: Condens. Matter **21** (2009) 245401 (8pp) doi:10.1088/0953-8984/21/24/245401

Vibrational properties of hexagonal $Ge_2Sb_2Te_5$ from first principles

G C Sosso[1], S Caravati[1,2], C Gatti[3], S Assoni[3] and M Bernasconi[1,4]

[1] Dipartimento di Scienza dei Materiali, Università di Milano-Bicocca, Via R Cozzi 53, I-20125, Milano, Italy
[2] Department of Chemistry and Applied Biosciences, ETH Zurich, USI Campus, Via Giuseppe Buffi 13, CH-6900 Lugano, Switzerland
[3] CNR-ISTM, c/o Dipartimento di Chimica Fisica ed Elettrochimica, Via Golgi 19, I-20133 Milano, Italy
[4] CNISM, Università di Milano-Bicocca, Via R Cozzi 53, I-20125 Milano, Italy

Received 29 January 2009, in final form 6 April 2009
Published 21 May 2009
Online at stacks.iop.org/JPhysCM/21/245401

Abstract

Phonons at the Γ point and the Raman spectrum of the hexagonal $Ge_2Sb_2Te_5$ were computed within density functional perturbation theory. The three different stackings of the Ge/Sb planes proposed in the experimental literature were considered. The theoretical Raman spectrum is similar for the three stackings with a marginally better agreement with experiments for the structure proposed by Matsunaga *et al* (2004 *Acta Crystallogr.* B **60** 685) which assumes a disorder in Ge/Sb site occupation. Although the large broadening of the experimental Raman peaks prevents discriminating among the different stackings, the assignment of the Raman peaks to specific phonons is possible because the main features of the spectrum are rather insensitive to the actual distribution of atoms in the Sb/Ge sublattices. On the basis of the energetics (including configurational entropy) two stackings seem plausible candidates for GST, but only the mixed stacking by Matsunaga *et al* reproduces the spread of Ge/Sb–Te bond lengths measured experimentally.

S Supplementary data files are available from stacks.iop.org/JPhysCM/21/245401

(Some figures in this article are in colour only in the electronic version)

1. Introduction

Phase change materials based on chalcogenide alloys are presently used in optical storage devices (DVDs) and are promising materials for non-volatile electronic memories [1–3]. Both applications rely on the reversible and fast transition between the amorphous and crystalline phases which have different optical and electronic properties. Among the chalcogenide glasses, $Ge_2Sb_2Te_5$ (GST) is the material of choice for non-volatile memory applications due to its superior performance in terms of speed of transformation and stability of the amorphous phase. In spite of the great technological importance of GST several issues on the microscopic structures of the crystalline and amorphous phases are still a matter of debate [3, 4]. GST has two crystalline phases, a metastable cubic (NaCl-like) phase which undergoes the reversible crystal-to-amorphous transition and a stable hexagonal phase [5–7]. The hexagonal phase has $P\bar{3}m1$ symmetry and nine atoms per unit cell in nine layers stacked along the c axis. Two different sequences have been proposed, namely the ordered stacking (hereafter referred to as stacking or phase A) Te–Ge–Te–Sb–Te–Te–Sb–Te–Ge [6] (figure 1) and the ordered stacking (referred to as B hereafter) Te–Sb–Te–Ge–Te–Te–Ge–Te–Sb [7] (figure 1). Most recent diffraction measurements suggested, however, a disordered phase with Sb and Ge randomly occupying the same layer (stacking or phase C hereafter) [5]. Calculations based on density functional theory (DFT) with gradient corrected exchange and correlation functional [8] revealed that stacking A has the lowest energy [9]. However, the difference in energy between phases A and C reported in [9] (2 meV/atom) is of the same order of magnitude expected for the free energy contribution (at 300 K) due to the configurational entropy of the disordered phase C ($\frac{4}{9}k_BT\ln 2 = 8$ meV/atom). Moreover, the weak binding in the Te–Te link might be very sensitive to the choice of the exchange and correlation functional. In this paper, we investigate further by *ab initio* calculations the different stackings proposed for hexagonal GST and the

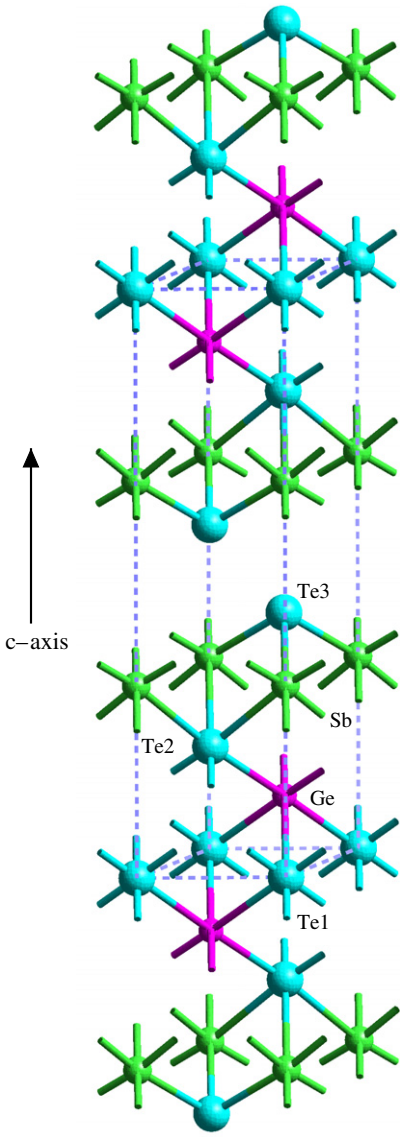

Figure 1. Structure of $Ge_2Sb_2Te_5$ in the hexagonal cell (stacking A, see text). Two formula units along the *c* axis, and period replica of atoms at the edges of the hexagonal cell in the *ab* plane are shown. Atoms independent by symmetry are labeled. In stacking B, the positions of Ge and Sb atoms are interchanged. The weak Te–Te bonds (3.7 Å long) connecting adjacent slabs are not shown to emphasize the presence of $Ge_2Sb_2Te_5$ stacks.

possibility to discriminate among them by looking at their vibrational properties. Phonons and Raman spectra were computed within density functional perturbation theory [10] and compared with the experimental Raman spectrum [11] aiming at assigning experimental Raman peaks to specific phonons which is of importance for the monitoring by Raman spectroscopy of the structural transformations [12] of relevance for the technological applications of this material.

2. Computational details

Calculations were performed within the framework of DFT with the exchange and correlation energy functional in the generalized gradient approximation (GGA) of Perdew–Becke–Ernzerhof (PBE [13]) and norm-conserving pseudopotentials, as implemented in the codes PWSCF and PHONON [14]. Only the outermost s and p electrons were considered in the valence. Kohn–Sham (KS) orbitals were expanded in a plane waves basis up to a kinetic cutoff of 20 Ryd. Brillouin zone (BZ) integration was performed over an $8 \times 8 \times 2$ Monkhorst–Pack (MP) mesh [15]. Equilibrium geometries were obtained by optimizing internal structure and lattice parameters. Residual anisotropy in the stress tensor at the optimized lattice parameters at each volume was below 0.4 kbar. The energy versus volume data were fitted with a Murnaghan function [16]. In the geometry optimization we first imposed the $P\bar{3}m1$ symmetry for phases A and B. As discussed in section 3.2, phase A turned out to be unstable in the $P\bar{3}m1$ symmetry due to a single soft mode. We therefore repeated all geometry optimizations by relaxing symmetry constraints. However, as discussed in section 3.2, the double-well potential along the soft mode is very shallow and the instability (at zero temperature) can be removed by phonon renormalization at room temperature. Therefore the structural and vibrational properties for phase A reported hereafter refer to the geometry optimized with the $P\bar{3}m1$ symmetry constraint.

3. Results

3.1. Structural and electronic properties

Firstly, we have optimized the internal structure of phases A, B and C at the experimental lattice parameters of [6] $a = 4.25$ Å and $c = 17.27$ Å, which are very close to the values of $a = 4.2247$ Å and $c = 17.2391$ Å in [5]. The disordered phase C was modeled by doubling the unit cell along *b* and putting one Ge and one Sb atom on each Ge/Sb layer (18-atom supercell). The geometry chosen for phase C corresponds to the best quasi-random structure compatible with an 18-atom supercell [17]. The resulting energies, atomic positions of atoms independent by symmetry and bond lengths of the relaxed structures are reported in table 1. Atomic positions for phase C are given in Annex 1 as additional material[5]. It turns out that phase A is the lowest in energy, in agreement with previous calculation [9]. However, the difference in energy between stacking A and the disordered phase C is of the same order of magnitude of the free energy gain due to disorder expected for phase C at 300 K (of the order of 8 meV/atom $= \frac{4}{9}k_B T \ln 2$). The Ge–Te bonds have a large spread in lengths (0.177–0.198 Å) in phases B and C, in agreement with experimental diffraction data [5], while the spread is negligible in phase A. In phases B and C, the octahedral environment of Ge is strongly distorted with the formation of two sets of bond lengths, three shorter and three longer bonds as in the trigonal ground state of the binary compound GeTe [18]. Similar results for phases A and B have been obtained in previous *ab initio* work [19]. On the basis of the energetics (including configurational entropy) both stackings A and C seem plausible candidates for GST, but only

[5] See Annexes 1–4 for the positions of atoms independent by symmetry of phase C (Annex 1) and for the displacement patterns of phases A (Annex 2), B (Annex 3) and C (Annex 4) available from stacks.iop.org/JPhysCM/21/245401.

Table 1. Relative energies (meV/atom) and bond lengths (Å) for phases A, B and C at the experimental lattice parameters $a = 4.25$ Å and $c = 17.27$ Å [6] (very close to the lattice parameters $a = 4.225$ Å and $c = 17.239$ Å of [5]) with the PBE functional. Values obtained with the B3PW hybrid functional are given in parentheses. Positions of atoms independent by symmetry (crystallographic units) are given here for phases A and B and as additional material (see footnote 5) for the larger unit cell of phase C.

	Stacking			
	A	B	C	
Energy	0 (3)	17 (12)	4 (0)	
	Bond length (Å)			Exp.[a]
Sb–Te	3.00–3.18 (2.98–3.17)	3.01–3.16 (2.99–3.14)	2.92–3.21 (2.90–3.24)	2.89–3.19
Ge–Te	2.98–3.00 (2.97–2.99)	2.83–3.22 (2.82–3.21)	2.86–3.21 (2.83–3.23)	2.89–3.19
Te–Te	3.84 (3.83)	3.71 (3.73)	3.63–3.83 (3.65–3.80)	3.75

Atomic positions							
Atom [A]	x	y	z [A]	z [B]	Atom [B]	Exp.[a]	Atom [Exp.[a]]
Te1	0	0	0	0	Te1	0	Te1
Ge	2/3	1/3	0.0999	0.1153	Sb	0.1061	Ge/Sb
Te2	1/3	2/3	0.1974	0.2162	Te2	0.2065	Te2
Sb	0	0	0.3145	0.3373	Ge	0.3265	Sb/Ge
Te3	2/3	1/3	0.4145	0.4192	Te3	0.4173	Te3

[a] Experimental data are from [5].

stacking C reproduces the spread of Ge/Sb–Te bond lengths measured experimentally. Moreover, the hierarchy in energy between stackings A and C depends on the choice of the exchange and correlation functional. Indeed, by repeating the geometry optimization at the experimental lattice parameters with the B3PW hybrid functional [20][6], it turns out that phase C is the lowest in energy with negligible changes in the internal structure with respect to the PBE results (cf table 1).

For stackings A and B, we also optimized the lattice parameters at the PBE level within the framework of section 2. The c/a ratio was optimized at each volume and the energy versus volume data were fitted by a Murnaghan function [16]. Residual anisotropy in the stress tensor at the optimized lattice parameter at each volume was below 0.4 kbar. The dependence of the c/a ratio as a function of the volume is reported in figure 2. Structural parameters at the theoretical equilibrium volume for phases A and B are reported in table 2. The same comments reported above for table 1 hold here. In addition, we must note an expansion of the lattice parameter c with respect to experiments which results in a sizable misfit in the Te–Te bond length, much larger than the usual errors within DFT–GGA. Our results are consistent with those reported in [22], but are in contrast with previous results by Sun *et al* [9] which show a contraction of the c parameter with respect to experiments ($a = 4.295(4.270)$ Å and $c = 16.977(17.172)$ Å, for phase A (B) in the theoretical work of [9]). The Te–Te bond lengths are brought into better agreement with experiments by fixing the lattice parameters to the experimental values (table 1). The misfit might be ascribed to deficiencies of the most common DFT–GGA functionals in describing weak bonds such as the Te–Te bond in this system.

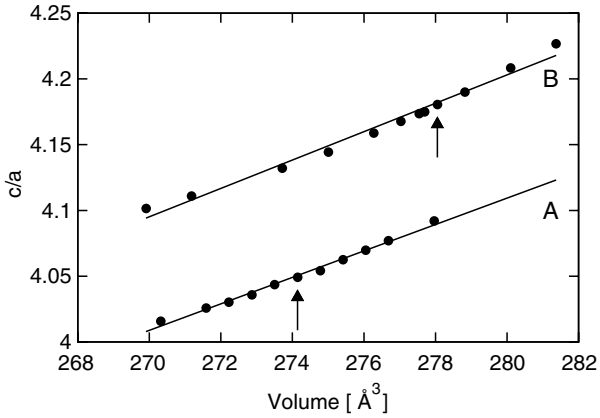

Figure 2. Theoretical c/a ratio as a function of volume (per formula unit) for phases A and B. Values at the theoretical equilibrium volumes are marked by arrows.

The calculated electronic density of state of GST at the theoretical equilibrium volume is reported in figure 3(a) for the three stackings. Phase A is semiconducting while phases B and C are metallic with a pronounced minimum at the Fermi level (both at the experimental and theoretical equilibrium lattice parameters). Metallicity originates from band crossing close to the Γ and A points of the BZ, as shown in the electronic band structure of phase B reported in figure 3(b). Similar results for phases A and B have been found in previous *ab initio* works [19, 23]. Experimentally, the hexagonal phase shows metallic character, the conductivity decreasing by increasing temperature [24]. However, as occurs in other chalcogenide compounds [25], GST is expected to display a large concentration of defects in stoichiometry (vacancy) which might induce a shift of the Fermi level, turning the system into a degenerate p-type semiconductor.

[6] The B3PW calculations were performed with a Gaussian-type DZVP basis set and Hay–Wadt small-core effective core pseudopotentials (ECP) as implemented in the code CRYSTAL [21]. Brillouin zone integration was performed with 8 (4) special points in the irreducible wedge for phases A and B (C). We checked that the changes with respect to PBE data in table 1 are not due to the different basis set/pseudopotentials by repeating PBE calculations with the CRYSTAL code.

Table 2. Relative energies (meV/atom) and bond lengths (Å) for phases A and B at the theoretical equilibrium lattice parameters (Å). Positions of atoms independent by symmetry (crystallographic units) are also given.

	Stacking		
	A	B	Exp.[a]
Energy (meV/atom)	0	19	
Cell parameters (Å)			
a	4.28	4.25	4.225
c	17.31	17.74	17.239
Bond length (Å)			
Sb–Te	3.01–3.19	3.01–3.17	2.89–3.19
Ge–Te	2.99–3.01	2.83–3.28	2.89–3.19
Te–Te	3.92	3.92	3.75

Atomic positions

Atom [A]	x	y	z [A]	z [B]	Atom [B]	Exp.[a]	Atom [Exp.[a]]
Te1	0	0	0	0	Te1	0	Te1
Ge	2/3	1/3	0.0995	0.1132	Sb	0.1061	Ge/Sb
Te2	1/3	2/3	0.1966	0.2117	Te2	0.2065	Te2
Sb	0	0	0.3131	0.3337	Ge	0.3265	Sb/Ge
Te3	2/3	1/3	0.4123	0.4138	Te3	0.4173	Te3

[a] Experimental data are from [5].

3.2. Vibrational properties

We computed the Raman spectrum from phonons at the Γ point within density functional perturbation theory [10] for the geometries optimized at the experimental lattice parameters (cf table 3). The differential cross section for Raman scattering (Stokes) in non-resonant conditions is given by (for a unit volume of scattering sample)

$$\frac{\mathrm{d}^2\sigma}{\mathrm{d}\Omega\,\mathrm{d}\omega} = \sum_j \frac{\omega_S^4}{c^4}|\mathbf{e}_S \cdot \underline{\underline{R}}^j \cdot \mathbf{e}_L|^2(n_\mathrm{B}(\omega/k_\mathrm{b}T)+1)\delta(\omega-\omega_j), \tag{1}$$

where $n_\mathrm{B}(\omega/k_\mathrm{b}T)$ is the Bose factor, ω_S is the frequency of the scattered light, and $\mathbf{e}_\mathrm{S}$ and $\mathbf{e}_\mathrm{L}$ are the polarization vectors of the scattered and incident light, respectively. The Raman tensor $\underline{\underline{R}}^j$ associated with the jth phonon is given by

$$R^j_{\alpha\beta} = \sqrt{\frac{V_o\hbar}{2\omega_j}}\sum_{\kappa=1}^{N}\frac{\partial\chi^\infty_{\alpha\beta}}{\partial\mathbf{r}(\kappa)}\cdot\frac{\mathbf{e}(j,\kappa)}{\sqrt{M_\kappa}}, \tag{2}$$

where V_o is the unit cell volume, $\mathbf{r}(\kappa)$ is the position of the κth atom and $\underline{\underline{\chi}}^\infty = (\underline{\underline{\varepsilon}}^\infty - \mathbf{1})/4\pi$ is the electronic susceptibility. The tensors $\underline{\underline{R}}^j$ were computed from $\underline{\underline{\chi}}^\infty$ by finite differences, by moving the atoms independent by symmetry with a maximum displacement of 0.01 Å. This is possible in a rigorous way only for insulating phases, i.e. for stacking A only. However, stackings B and C have a very low density of states at the Fermi level originating from states at specific points in the BZ (Γ and A). By performing the BZ integration over the $8\times8\times2$ mesh, the k-points are sufficiently far from the Γ and A points so that phases B and C also behave as insulators which allows computing the Raman tensors for these latter phases as well. However, we must consider that in these latter cases larger errors in the Raman cross section are also possible, because of possible resonance effects with the laser probe (in a zero-gap system) neglected in equation (1).

For the ordered phases A and B, phonons at the Γ point are classified according to the irreducible representations of the point group D_{3d} as $\Gamma = 4(A_{1g}+E_g+E_u+A_{2u})$. The disordered phase C would still display the D_{3d} symmetry by averaging out the difference between Ge and Sb. In our particular representation of the disordered phase C in a 18-atom supercell, symmetry is partially broken when Ge and Sb are taken as distinct species as they are; the C_s symmetry is preserved and the modes at the Γ point have A' and A'' character (all Raman-active). Calculated frequencies of Γ-point phonons for phases A and B are given in table 3 for the optimized geometry at the experimental equilibrium lattice parameters [6]. The effect of the change in the lattice parameters from the experimental to the theoretical values at equilibrium is overall small with a maximum shift of 6 cm^{-1} in phonon frequencies. Phonon frequencies for the disordered phase C at the Γ-point are given in graphical form in figure 4. Note that there is an unstable mode of E_u symmetry in phase A (negative frequency). This mode corresponds to an in-phase shift of the two Ge layers along a which breaks the $P\bar{3}m1$ symmetry imposed during geometry optimization. The instability is confirmed by a frozen phonon calculation which revealed the presence of a double-well potential with the two minima separated by a very tiny barrier of 0.118 meV/cell which could be easily overcome at room temperature. Therefore, the instability should be removed at finite temperature by a renormalization of the phonon frequency. Zero-point energy corrections (from Γ-point phonons only) for phases A (with the unstable phonon omitted), B and C are 4.805, 5.384 and 5.524 meV/atom, respectively, and do not change the hierarchy in energy discussed previously. The Raman tensor (equation (2)) for the

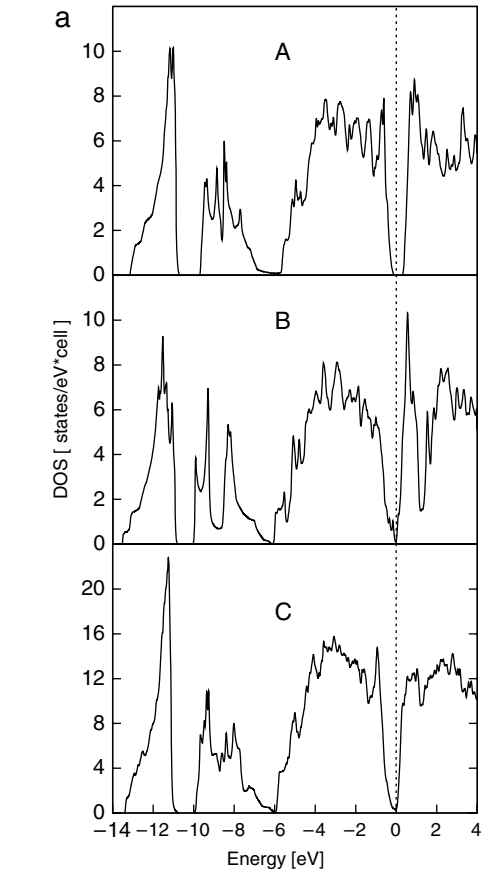

Figure 3. (a) Electronic density of states of phases A, B and C at the theoretical equilibrium lattice parameters, calculated by the tetrahedron method over a $14 \times 14 \times 14$ MP mesh in the irreducible BZ. (b) Band structure of phase B along high symmetry directions in the irreducible BZ. The zero of energy is the Fermi level.

Raman-active irreducible representations of the D_{3d} group (all the g modes) has the following form [26]:

$$A_{1g} \Rightarrow \begin{bmatrix} a & . & . \\ . & a & . \\ . & . & b \end{bmatrix}$$

$$E_g(x) \Rightarrow \begin{bmatrix} c & . & . \\ . & -c & d \\ . & d & . \end{bmatrix} \qquad (3)$$

$$E_g(y) \Rightarrow \begin{bmatrix} . & -c & -d \\ -c & . & . \\ -d & . & . \end{bmatrix}.$$

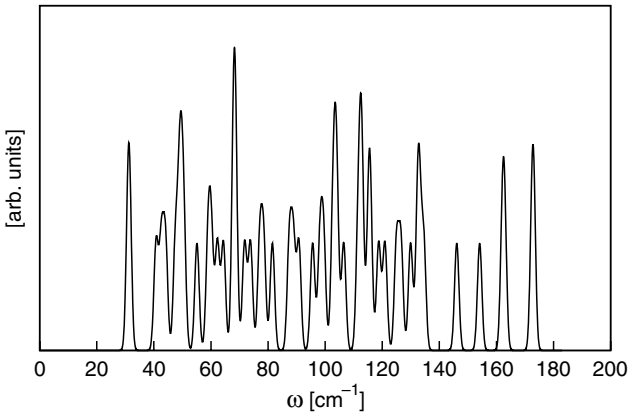

Figure 4. Phonons at the Γ-point of phase C. Each energy level is broadened with a Gaussian function 0.3 cm^{-1} wide.

The calculated coefficients of the Raman tensors for phases A and B are given in table 3. In our representation of phase C, the Raman tensors do not satisfy the D_{3d} symmetry due to the symmetry-breaking-induced Ge/Sb disorder in our finite supercell. The experimental Raman spectrum for polycrystalline sample in backscattering geometry and unpolarized light [11] is compared with the theoretical spectra for phases A, B and C in figure 7. The δ functions in equation (1) are approximated by Lorentzian functions with a constant width of 4 cm^{-1}. The total cross section for a polycrystalline sample and unpolarized light in backscattering geometry is obtained from equation1with the substitution [26]

$$4(R_{xx}^2 + R_{yy}^2 + R_{zz}^2) + 7(R_{xy}^2 + R_{xz}^2 + R_{yz}^2) + (R_{xx}R_{yy} + R_{xx}R_{zz} + R_{zz}R_{yy}) \rightarrow 30|\mathbf{e}_S \cdot \underline{\underline{R}}^j \cdot \mathbf{e}_L|^2. \quad (4)$$

In phases A and B, modes A_{1g} and E_g correspond to atomic displacement along and perpendicular to the c axis (normal to the hexagonal planes), respectively. Displacement patterns of Raman-active phonons in phases A and B are given in figures 5 and 6. Full sets of displacement patterns for phases A, B and C are given in Molden format as additional material (see footnote 5). Symmetry breaking due to Ge/Sb disorder in phase C makes several modes active in the Raman spectrum and induces a mixing of the displacements along and perpendicular to the c axis. Nevertheless, the modes keep a predominant A-like or E-like character also in phase C. To easily identify the type of displacement patterns responsible for the Raman peaks, we report in figure 8 the Raman spectra for phases A, B and C projected on Te, Sb and Ge atoms (by multiplying the Raman tensors (equation (2)) by $\sum_\kappa \frac{|\mathbf{e}(j,\kappa)|^2}{M_k}$, where the sum over κ is restricted to atoms of a given species). For phase C, the Raman spectrum is also projected on displacement along or perpendicular to the c axis (figure 8(b)) which allows assigning a dominant E-like (vibrations in the ab plane) or A-like (vibrations along c) to Raman-active phonons of phase C.

The peaks in the range 90–120 cm^{-1} for all the three stackings are due to E-type modes (vibrations in the ab plane) while the peaks above 150 cm^{-1} are due to A-type phonons (vibrations along c) (see figure 8(b) for phase C). The larger broadening of the structure around 100 cm^{-1} in phase C

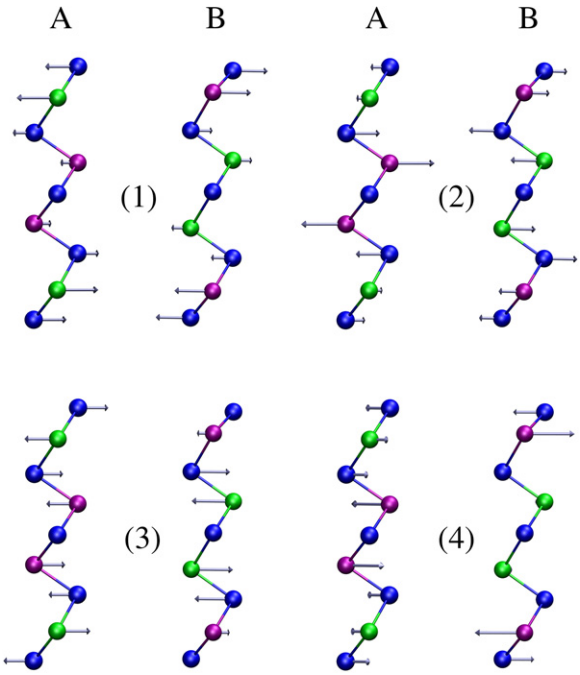

Figure 5. Sketch of the displacement patterns of Raman-active E_g phonons at the Γ-point for phases A and B. Displacements in the *ab* plane are involved.

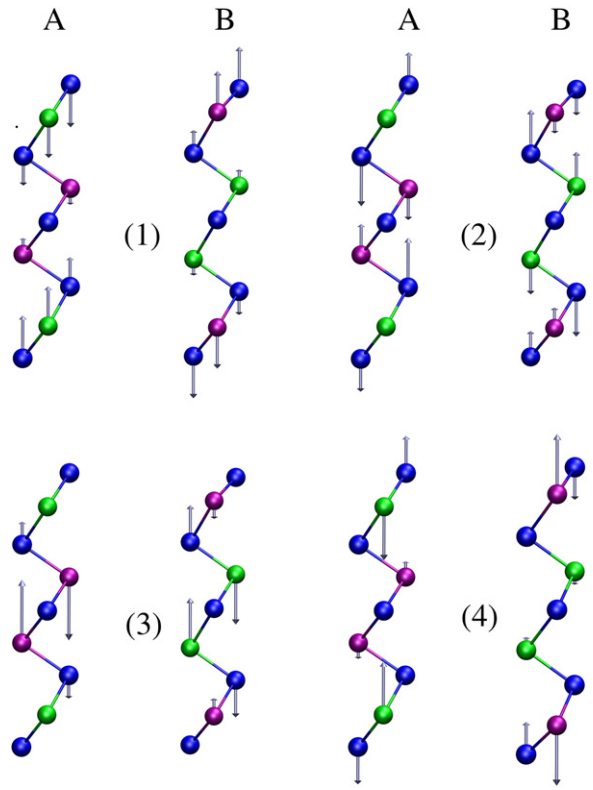

Figure 6. Sketch of the displacement patterns of Raman-active A_{1g} phonons at the Γ-point for phases A and B. Displacements along the *c* axis are involved.

Table 3. Frequency (cm^{-1}) of g-mode (Raman-active) phonons of the optimized geometry at experimental equilibrium lattice parameters for stackings A and B. The u modes (IR-active) are reported separately. Acoustic modes (at zero frequency) are omitted. The coefficients of the Raman tensor (equation (2) and matrices (3)) are reported in units of 10^{-4} $Å^3$ for stackings A and B.

g-modes	ω	a^2 (c^2)	b^2 (d^2)
Stacking A			
$E_g(1)$	29	1.19	0.92
$A_{1g}(1)$	40	4.74	57.44
$E_g(2)$	77	1.26	0.51
$A_{1g}(2)$	97	6.24	31.49
$E_g(3)$	100	6.75	28.52
$E_g(4)$	117	1.10	21.09
$A_{1g}(3)$	156	0.19	0.18
$A_{1g}(4)$	166	10.94	26.17
E_u	−9, 51, 102, 111		
A_{2u}	67, 107, 119, 166		
Stacking B			
$E_g(1)$	35	2.67	0.87
$A_{1g}(1)$	47	0.34	3.53
$E_g(2)$	53	0.68	2.34
$A_{1g}(2)$	74	7.18	0.05
$E_g(3)$	100	54.80	44.35
$E_g(4)$	143	11.41	4.66
$A_{1g}(3)$	161	45.05	6.03
$A_{1g}(4)$	179	17.81	2.55
E_u	35, 92, 100, 141		
A_{2u}	48, 112, 146, 179		

is partially due to the symmetry breaking which splits the degenerate E modes. Surprisingly enough, in all phases A, B and C the Raman-active mode at the highest frequency is a A-like mode modulating the outermost (closer to Te–Te linkage) Te–X bond, irrespective of the nature of X which is Ge in phase B, Sb in phase A and a mixed Sb/Ge layer in phase C. Furthermore, for phases A and B, the modes with the same label (but for $E_g(4)$) have very similar displacement patterns irrespective of the presence of Ge or Sb in a particular site which means that the frequency of the mode is controlled more by the position of the atoms (Ge, Sb) involved in the vibrations than by the chemical identity of the vibrating atoms themselves. It is interesting to compare the displacement patterns depicted in figures 5 and 6 with those of Sb_2Te_3 that we computed previously within the same theoretical framework used here [27]. The building blocks of crystalline Sb_2Te_3 can ideally be obtained from stacking B by removing the two outermost Ge and Te layers from the slab (Te–Sb–Te–Sb–Te). Modes $E_g(2)$ (53 cm^{-1}), $E_g(3)$ (100 cm^{-1}), $A_{1g}(2)$ (74 cm^{-1}) and $A_{1g}(3)$ (166 cm^{-1}) of stacking B show frequency and displacement patterns for the inner Te–Sb–Te–Sb–Te subunit which closely correspond to those of the modes $E_g(1)$ (49 cm^{-1}), $E_g(2)$ (117 cm^{-1}), $A_{1g}(1)$ (67 cm^{-1}) and $A_{1g}(2)$ (169 cm^{-1}) of crystalline Sb_2Te_3 [27], respectively. Phase A shows a strong Raman peak at ∼40 cm^{-1} which is not present in phases B and C and which might be the experimental fingerprint of phase A. Unfortunately, no experimental data are available below 90 cm^{-1}. Note that in the experimental work by Liu *et al* [11] the peak at 99 cm^{-1} was assigned to phonons modulating Ge–Te or Sb–Te bonds while the peak at 160 cm^{-1} was erroneously assigned to Sb–Sb stretching

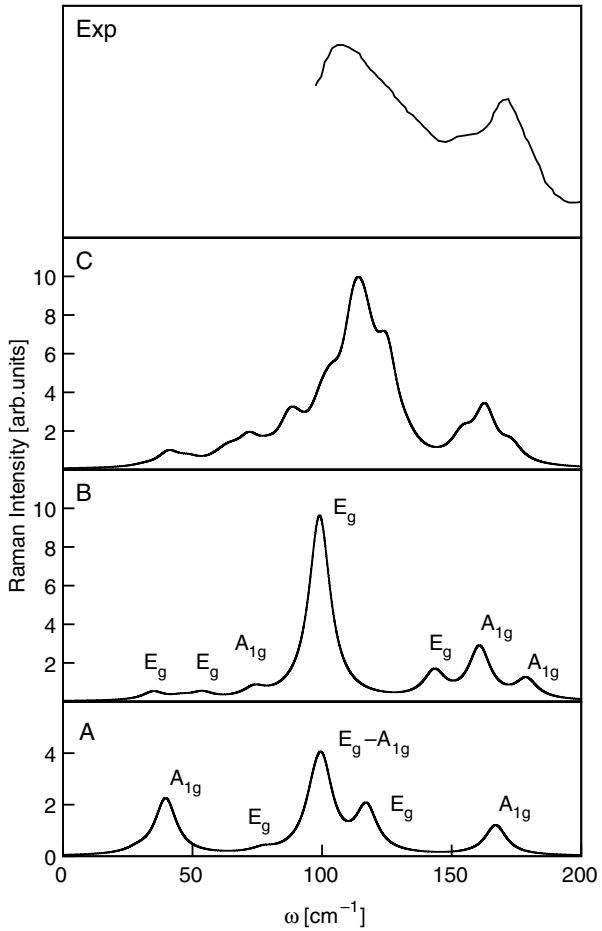

Figure 7. Experimental Raman spectrum for polycrystalline hexagonal $Ge_2Sb_2Te_5$ in backscattering geometry and unpolarized light [11], compared with theoretical spectra at 300 K for phases A, B and C from equations (1) and (2). The δ functions in equation (1) are approximated by Lorentzian functions with a constant width of 4 cm^{-1}. One A_{1g} mode in phases A and B and one E_g mode in phase A have very low Raman activity and are not resolved in the Raman spectra (cf table 3). The Bose factor in equation (1) is omitted.

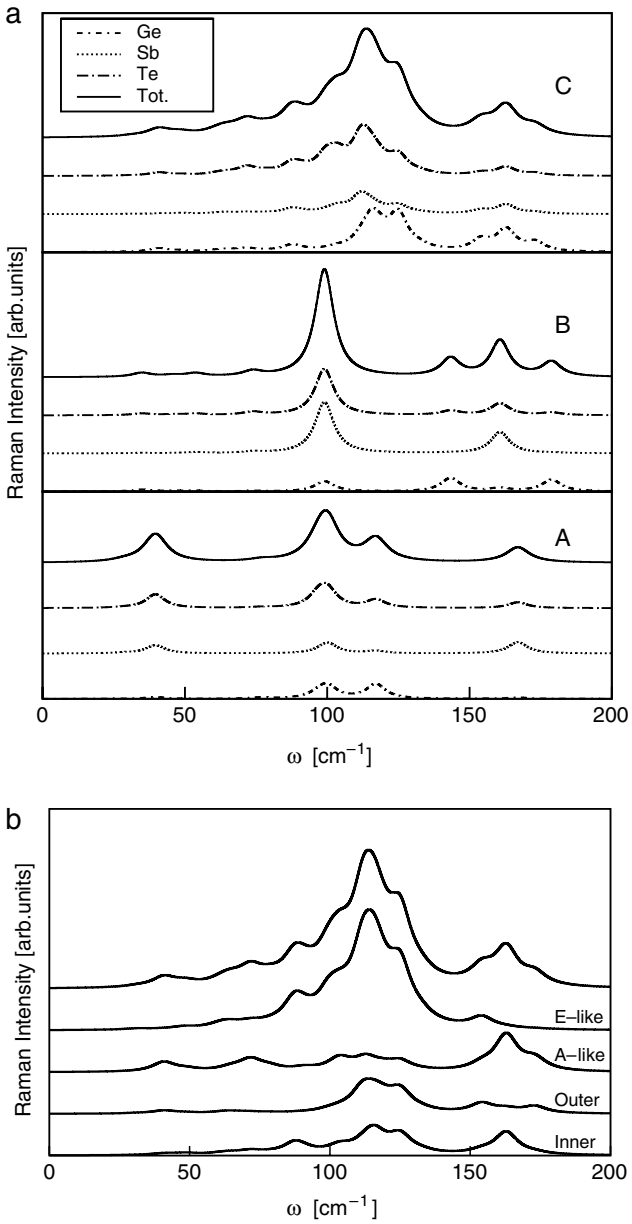

Figure 8. (a) Theoretical Raman spectra of phases A, B and C projected on the different species (see text). (b) Theoretical Raman spectrum of phase C projected on displacements perpendicular (E-like) and parallel (A-like) to the *c* axis. Raman spectra projected on the two Ge/Sb (outer) planes closer to the Te–Te linkages or on the other two inner planes (inner) are also shown. The Bose factor in equation (1) is omitted.

modes in antisite defects. Overall the Raman spectrum of phase C seems more similar to the experimental spectrum than those of phases A and B, although we cannot rule out that line broadening due to electron–phonon coupling (in the metallic phases), anharmonic effects and resonance conditions with the laser probe (all neglected in the theoretical spectra), might bring the Raman spectra of phases A or B in better agreement with experiments. Moreover, coherent phonon spectroscopy of hexagonal GST [28] revealed the presence of a dominant mode at 50 cm^{-1} and two weaker modes at 100 and 170 cm^{-1} which should correspond to Raman-active modes. For phase C, we indeed find Raman peaks at ∼45, 102 and 170 cm^{-1} (cf figure 7) which can be assigned to the peaks in the experimental coherent phonon spectrum.

4. Conclusions

Based on density functional perturbation theory, we computed the Raman spectrum of $Ge_2Sb_2Te_5$ in the hexagonal crystalline phases. We considered the three different stacking geometries proposed in the literature [5–7] (stackings A, B and C). The disordered structure proposed by Matsunaga *et al* [5] was modeled by an 18-atom supercell in which one Ge and one Sb atom occupy the two lattice sites on each Ge/Sb layer of the supercell (stacking C). The lowest energy phase A does not display the spread in Ge/Sb–Te bond lengths measured experimentally, which is reproduced instead by phases B ad C. Moreover, phase C is only marginally higher in energy than phase A, within the free energy contribution expected for configurational disorder, and even marginally

lower in energy than phase A if the hybrid B3PW functional is adopted. The theoretical Raman spectra of the three phases are similar, with phase C reproducing marginally better the experimental spectrum [11]. However, due to the large broadening of the experimental Raman peaks and possible theoretical uncertainties, the Raman spectrum does not seem sufficient to discriminate among the proposed stackings, but for a strong Raman peak at $\sim$40 cm^{-1}, outside the experimental range measured experimentally so far, which is present only for stacking A. Nevertheless, the assignment of the experimental Raman peaks to specific phonons we provide is rather insensitive to the actual distribution of Ge/Sb atoms.

Acknowledgments

The authors gratefully acknowledge the computer resources, technical expertise and assistance provided by the Barcelona Supercomputing Center–Centro Nacional de Supercomputación, by the DEISA Consortium under project PHASEMAT, and by CSCS (Manno, CH). Discussions with E Bonera are gratefully acknowledged. The Fondazione CARIPLO is gratefully acknowledged for partially supporting this research through project 2005-1245.

References

[1] Pirovano A, Lacaita A L, Benvenuti A, Pellizzer F and Bez R 2004 *IEEE Trans. Electron Devices* **51** 452
[2] Lacaita A L and Wouters D J 2008 *Phys. Status Solidi* a **205** 2281
[3] Wuttig M and Yamada N 2007 *Nat. Mater.* **6** 824
[4] Welnic W and Wuttig M 2008 *Mater. Today* **11** 20
[5] Matsunaga T, Yamada N and Kubota Y 2004 *Acta Crystallogr.* B **60** 685
[6] Kooi B J and De Hosson T M J 2002 *J. Appl. Phys.* **92** 3584
[7] Petrov I I, Imanov R M and Pinsker Z G 1968 *Sov. Phys.—Crystallogr.* **13** 339
[8] Perdew J P and Wang Y 1992 *Phys. Rev.* B **45** 13244
[9] Sun Z, Zhou J and Ahuja R 2006 *Phys. Rev. Lett.* **96** 055507
[10] Baroni S, de Gironcoli S, Dal Corso A and Giannozzi P 2001 *Rev. Mod. Phys.* **73** 515
[11] Liu B, Song Z-T, Zhang T, Feng S-L and Chen B 2004 *Chin. Phys.* **13** 1947
[12] De Bastiani R, Piro A M, Grimaldi M G, Rimini E, Baratta G A and Strazzulla G 2008 *Appl. Phys. Lett.* **92** 241925
[13] Perdew J P, Burke K and Ernzerhof M 1996 *Phys. Rev. Lett.* **77** 3865
[14] Baroni S, dal Corso A, de Gironcoli S and Giannozzi P *Pwscf and Phonons* http://www.pwscf.org
[15] Monkhorst H J and Pack J D 1976 *Phys. Rev.* B **13** 5188
[16] Murnaghan D 1944 *Proc. Natl Acad. Sci. USA* **30** 224
[17] Zunger A, Wei S H, Ferreira L G and Bernard G E 1990 *Phys. Rev. Lett.* **65** 353
[18] Goldak J, Barrett C S, Innes D and Youdelis W 1966 *J. Chem. Phys.* **44** 3323
[19] Lee G and Jhi S-H 2008 *Phys. Rev.* B **77** 153201
[20] Becke A D 1993 *J. Chem. Phys.* **77** 5648
Perdew J P and Wang W 1992 *Phys. Rev.* B **45** 13244
[21] Dovesi R, Saunders V R, Roetti C, Orlando R, Zicovich-Wilson C M, Pascale F, Civalleri B, Doll K, Harrison N M, Bush I J, D'Arco Ph and Llunell M 2006 *CRYSTAL06 User's Manual* (Torino: University Torino)
[22] Da Silva J L F, Walsh A and Lee H 2008 *Phys. Rev.* B **78** 224111
[23] Yamanaka S, Ogawa S, Morimoto I and Ueshimi Y 1998 *Japan. J. Appl. Phys.* **37** 3327
[24] Lee B-S, Abelson J R, Bishop S G, Kang D-H, Cheong B-K and Kim K-B 2005 *J. Appl. Phys.* **97** 093509
[25] Edwards A H, Pineda A C, Schultz P A, Martin M G, Thompson A P, Hjalmarson H P and Umrigar C J 2006 *Phys. Rev.* B **73** 045210
[26] Loudon R 2001 *Adv. Phys.* **50** 813
[27] Sosso G C, Caravati S and Bernasconi M 2009 *J. Phys.: Condens. Matter* **21** 095410
[28] Först M, Dekorsy T, Trappe C, Lurenzis M, Kurz H and Bechevet B 2000 *Appl. Rev. Lett.* **77** 1964